

Cite this: *Digital Discovery*, 2026, 5, 844

Molecular dynamics simulations accelerated on FPGA with high-bandwidth memory

Jing Xiao, ^{abc} Jinfeng Chen, ^{bcd} Ye Ding, ^{bc} You Xu ^{bc} and Jing Huang ^{*bcd}

Molecular dynamics (MD) simulation is a powerful tool for investigating complex systems in physical, materials, and biological sciences. However, computational speed remains a critical bottleneck that limits its broader application. To address this challenge, we developed a dedicated hardware module based on modern field-programmable gate arrays (FPGAs) that accelerates all components of MD simulations. Our design employs pipelining strategies to optimize task execution within a fully parallel architecture, significantly enhancing performance. The latest generation of high-bandwidth memory (HBM2) is integrated and optimized to improve computational throughput. At the hardware level, we implemented an optimized register-transfer level (RTL) circuit design for a single node to maximize the efficiency of register read and write operations. Software co-design with SIMD frameworks ensures seamless integration of force calculations and system propagation. We validated the implementation across systems ranging from argon gas to solvated proteins, demonstrating stable MD trajectories and close agreement with reference energy values. This work presents a novel FPGA-based MD simulation architecture and provides a foundation for further improvements in hardware-accelerated molecular simulations.

Received 1st September 2025

Accepted 6th January 2026

DOI: 10.1039/d5dd00391a

rsc.li/digitaldiscovery

1 Introduction

Due to their ability to provide detailed mechanistic insights into various physical interactions at the atomic level, molecular dynamics (MD) simulations have become paramount in driving the rational discovery of therapeutic agents and functional materials.^{1–4} However, functionally relevant processes are mostly driven by the collective motion of aggregated ensembles of molecules, which span large spatial scales and are computationally demanding to model comprehensively. Consider many-body systems interacting through classical pairwise potentials: the computational demand for integrating the equations of motion escalates rapidly with the number of interacting particles. Moreover, most biophysical activation processes of mechanistic interest occur over heterogeneous timescales.⁵ For example, essential cellular activities fundamental to life, such as active solute transport,^{6,7} can take place on sub-second timescales, while molecular vibrational motions are characterized on the femto- to picosecond scale. The multi-scale nature of these systems limits the time-step length to sufficiently short intervals (typically 0.5 to 4 femtoseconds) to

ensure stable dynamical integration, rendering the computational modeling of long-timescale collective molecular behaviors highly intensive.⁸

To extend the accessible simulation scales within the limits of modern computational hardware, contemporary MD implementations have adopted multi-CPU parallel strategies and GPU-based acceleration.^{9–13} However, even with GPU support, the trajectory lengths reported in most MD studies rarely exceed ten microseconds. Numerically propagating molecular trajectories for systems containing a few million particles can still require weeks of fully loaded computational power.¹⁴ While modern GPUs excel at regular computations, their architectures struggle with irregular memory-access patterns and unpredictable latency in large-scale MD simulations.

Beyond conventional CPU/GPU-based solutions, heterogeneous computing architectures have emerged as a promising paradigm for MD simulations. Recent implementations integrate microcontroller units (MCUs), field-programmable gate arrays (FPGAs),^{15–18} and complex programmable logic devices (CPLDs) through dedicated photonic interconnects, exemplified by the MD-GRAPe cluster architecture that achieves sub-microsecond communication latency between processing nodes.^{19,20} The commercial ANTON supercomputer series utilized the Application Specific Integrated Circuit (ASIC) processors to construct a specifically designed cluster with 64 or 512 nodes.^{21–23} However, these architectures are commercially expensive to implement, which limits their applicability for routine simulations. On the other hand, the Novo-G

^aFudan University, Shanghai, 200433, China^bState Key Laboratory of Gene Expression, School of Life Sciences, Westlake University, Hangzhou, Zhejiang, 310030, China. E-mail: huangjing@westlake.edu.cn^cWestlake AI Therapeutics Laboratory, Westlake Laboratory of Life Sciences and Biomedicine, Hangzhou, Zhejiang, 310024, China^dInstitute of Biology, Westlake Institute for Advanced Study, Hangzhou, Zhejiang, 310024, China

reconfigurable computing design leverages programmable hardware such as FPGAs to tackle the energy efficiency and performance bottlenecks, and have shown prominent potential for MD simulations.^{24,25}

Compared to alternative computing hardware, FPGAs offer greater design flexibility and improved environmental friendliness with competitive computational efficiency.^{26–29} FPGAs incorporate a variety of unique production techniques, such as the flash process and the reverse fusion process, which allow for multiple reconfigurations and debugging cycles in the commercial applications, accommodating diverse experimental design requirements.³⁰ During the chip development phase, FPGAs are often used as the core platform for prototyping, highlighting their potential for eventual translation into ASIC processes.^{31,32} With their high parallel capacity, reconfigurability, and excellent energy efficiency, FPGAs offer unique advantages for MD simulations. They can significantly accelerate compute-intensive floating-point operations by processing particle interaction forces, including van der Waals (vdW) and Coulomb forces, in parallel across thousands of configurable logic units. The pipelined hardware design of FPGAs enables efficient coordination of neighbor-list generation, force calculation, and integration. Moreover, FPGAs can be flexibly adapted to different potential functions and numerical integration schemes in MD simulations, thereby supporting a wide range of models from rigid bodies to coarse-grained systems.³³

FPGA fabrication technologies have advanced rapidly in recent years, with process nodes reaching 7 nm and below, enabling significant performance improvements in high-performance computing. In parallel, the introduction of high-bandwidth memory (HBM) addresses the longstanding data-throughput bottleneck in MD simulations,^{34,35} where force calculations demand sustained memory bandwidth exceeding 100 GB s^{-1} . Despite these advances, no existing FPGA-based MD implementations have yet taken advantage of HBM2's unique combination of bandwidth density and near-memory compute capabilities, leaving a critical gap in scaling MD simulations beyond 10-million-atom systems.

In this study, we report the co-design of both hardware and software components based on a hybrid CPU/FPGA architecture specifically developed for MD simulations using classical force fields (FFs) such as CHARMM36m.³⁶ To achieve optimal computational-load balancing, our design retains the bonded interaction calculations on the CPU while offloading the more computationally intensive non-bonded interaction evaluations to the FPGA. We present practical implementations of FPGA computing units specifically designed for scalable electrostatic interaction calculations based on the particle-mesh Ewald (PME) algorithm, using three-dimensional fast Fourier transform kernels. In addition, we introduce a Single Instruction, Multiple Data (SIMD) software framework developed to improve the circuit's data processing capabilities. The rest of the paper is organized as follows: Section 2 introduces the FPGA architecture used in our design and reviews the relevant algorithms in MD simulations, focusing on their implications for achieving optimal computing performance in practice. Section 3 details the algorithmic implementation on the FPGA hardware for

massively parallel non-bonded interaction computations, based on a Network-on-Chip (NoC) architecture and an HBM2 memory layout designed for efficient data dispatch with minimal memory overhead. Also presented in Section 3 is the validation of our hybrid hardware implementation on model systems with varying complexity, from argon particles to the DHFR protein in explicit solvent. Finally, Section 4 provides discussion and concluding remarks.

2 Methods

2.1 Hardware platform

This work employs the Inspur F37X FPGA accelerator card featuring the Xilinx Virtex UltraScale+ VU37P chip. Its programmable architecture enables dynamic reconfiguration of DSP blocks and hardware-level algorithm mapping, directly addressing the memory-wall bottleneck in traditional CPU architectures (*via* HBM2's 460 GB s^{-1} bandwidth supporting dataflow parallelism) and the inflexibility of fixed instruction sets. The card delivers 28.1 TOPS INT8 compute performance at 75 W power, demonstrating 44% higher energy efficiency than the NVIDIA A100 (19.5 TOPS at 250 W),³⁷ making it particularly suitable for deterministic-latency applications such as real-time signal processing. Comparative studies show that FPGA solutions achieve 3–8× lower tail latency than CPU/GPU hybrids for sparse matrix computations, although their stream computing advantages require careful balancing with batch-processing demands in scientific computing. This architecture ultimately addresses the joint optimization challenge of achieving high throughput and low latency through hardware-level customization (see SI Table S1 for quantified comparisons).

2.2 Classical MD simulation

A classical MD program can be divided into four parts:³⁸

1. Parse the specified simulation conditions, such as simulation temperature, particle number, time step, and topology of the simulation system.
2. Initialize the positions and velocities of the particles.
3. Compute the forces acting on all particles.
4. Integrate Newton's equations to update the velocities and positions of all particles.

Steps 3 and 4 are repeated until the user-specified number of simulation steps is reached. In classical MD simulations, the force acting on each atom is typically calculated using classical force fields.³⁹ Given the force acting on each particle, the velocity and position will be updated by an integrator algorithm, for example, the velocity Verlet methods. Most FFs model interactions between particles using bonded and non-bonded terms:

$$F_{\text{total}} = F_{\text{bonded}} + F_{\text{non-bonded}} \quad (1)$$

The bonded force consists of bond, angle, dihedral and improper terms:

$$F_{\text{bonded}} = F_{\text{bonds}} + F_{\text{angles}} + F_{\text{dihedrals}} + F_{\text{impropers}} \quad (2)$$



Most bonded terms are modeled by harmonic potentials, except for the dihedrals, which are modeled using a summation of cosine functions.³⁶ Because the bonded terms are only calculated when bonds exist between atoms, their computational cost can be regarded as $\mathcal{O}(N)$.

2.3 Non-bonded-force calculations

The non-bonded terms in classical FFs often consist of vdW interactions, represented by the Lennard-Jones (LJ) potential, and electrostatic interactions, modeled as Coulomb interactions between point charges:

$$F_i^{\text{LJ}} = \sum_{j \neq i} \frac{\epsilon_{ab}}{\sigma_{ab}^2} \left\{ 12 \left(\frac{\sigma_{ab}}{|\mathbf{r}_{ij}|} \right)^{14} - 6 \left(\frac{\sigma_{ab}}{|\mathbf{r}_{ij}|} \right)^8 \right\} \mathbf{r}_{ji} \quad (3)$$

$$F_i^{\text{Coulomb}} = \frac{q_i}{4\pi\epsilon} \sum_{j \neq i} \left\{ \frac{1}{|\mathbf{r}_{ij}|} \right\}^3 \mathbf{r}_{ji} \quad (4)$$

Here, ϵ_{ab} and σ_{ab} are particle interaction parameters. Since non-bonded forces must be computed between nearly all particle pairs, the computational cost is $\mathcal{O}(N^2)$. Thus, the primary bottleneck in MD simulations lies in the evaluation of non-bonded interactions.

Due to the slow decay of Coulomb forces with distance, they are typically computed using the PME algorithm under periodic boundary conditions (PBC) to efficiently handle long-range interactions. The algorithm partitions E^{Coulomb} into real-space and reciprocal-space contributions by introducing spherically distributed Gaussian charges of opposite signs. The total electrostatic energy of a system under PBC is expressed as:

$$E^{\text{Coulomb}} = \frac{1}{4\pi\epsilon} \sum_n \sum_{i>j}^N \sum_{j=1}^N \frac{q_i q_j}{|r_{ij} + nL|}. \quad (5)$$

Here we consider a cubic simulation box of length L , containing N charged particles. r_{ij} denotes the distance between particle i and particle j , and ϵ is the vacuum dielectric constant. The simulation lattice extends infinitely in all directions according to the PBC. The Gaussian distribution function is introduced into the Ewald summation algorithm and consists of three parts after being processed by the PME algorithm:

$$E^{\text{Coulomb}} = E_{\text{dir}} + E_{\text{rec}} + E_{\text{corr}}, \quad (6)$$

$$E_{\text{dir}} = \frac{1}{2} \sum_n \sum_{i,j=1}^N \frac{q_i q_j \text{erf}(\beta |\mathbf{r}_j - \mathbf{r}_i + \mathbf{n}|)}{|\mathbf{r}_j - \mathbf{r}_i + \mathbf{n}|}, \quad (7)$$

$$E_{\text{rec}} = \frac{1}{2\pi V} \sum_{\mathbf{m} \neq 0} \frac{\exp(-\pi^2 \mathbf{m}^2 / \beta^2)}{\mathbf{m}^2} S(\mathbf{m}) S(-\mathbf{m}), \quad (8)$$

$$E_{\text{corr}} = -\frac{1}{2} \sum_{(i,j) \in M} \frac{q_i q_j \text{erf}(\beta |\mathbf{r}_i - \mathbf{r}_j|)}{|\mathbf{r}_i - \mathbf{r}_j|} - \frac{\beta}{\sqrt{\pi}} \sum_{i=1}^N q_i^2, \quad (9)$$

where β is Ewald's coefficient, which regulates the speed of convergence of real space and Fourier space. The larger its value, the faster the real space converges and the slower the

Fourier space converges and *vice versa*. erf represents the Gaussian error function.

2.4 Neighbor list and its optimization

To improve efficiency, the calculation of short-range forces in real space sometimes uses a proximity-based lookup method to determine the spatial relationship between particles based on inter-particle distances. These relationships are stored in a neighbor list, which is periodically updated as the simulation progresses and particle positions change. For interactions within a short range (range-limited), each particle interacts only with nearby particles within a specified cutoff radius. The neighbor list is constructed by assigning each particle to a region in space and identifying neighboring particles within a cutoff distance r_{cut} . Each particle then maintains a list of potential neighbors, which serves as input to the next computational step.

In 3D periodic systems, each simulation cell has 26 adjacent cells. Newton's third law states that action and reaction forces are equal in magnitude but opposite in direction. In MD simulations, this implies that the interaction force between particle pair (i, j) satisfies $F_{ij} = -F_{ji}$. Accordingly, to avoid redundant force calculations, only the 13 neighboring cells in the upper half of the central cell are considered when filtering particle pairs, as illustrated in Fig. S1. Essentially, one can reduce computational overhead by calculating only half of the neighbor pairs while maintaining full force accuracy.

Furthermore, we can employ a modified Verlet neighbor list that stores only unidirectional particle pairs as a strategy for optimizing the neighbor list:

$$\text{Neighbor list} = \{(i, j) | i < j, r_{ij} < r_{\text{cut}} + r_{\text{buffer}}\} \quad (10)$$

where r_{ij} is the interatomic distance, r_{cut} is the cutoff radius, and r_{buffer} is the buffer distance (or "skin") used to reduce the frequency of list updates (see SI Fig. S2).

3 Results

3.1 Proposed architecture

Based on the MD algorithm, this work proposes an FPGA architecture for accelerating MD simulations. As an example, the range-limited (RL) module, which computes the vdW interactions and the real-space component of the electrostatic interactions, is illustrated in Fig. 1. The CPU first preprocesses the simulation data by assigning a unique identifier to each particle and partitioning the dataset based on cell indices, effectively defining the spatial decomposition of the system. Particle information is then associated with the corresponding cell serial numbers. The cell size is determined by the cutoff distance, and the number of cells depends on the dimensions of the simulation box. Each cell contains information not only about its own particles but also about particles in its neighboring cells. This information is organized into structured data tables stored in memory.

Each particle occupies one row in the storage space. The starting address of each data unit (cell) can be directly located



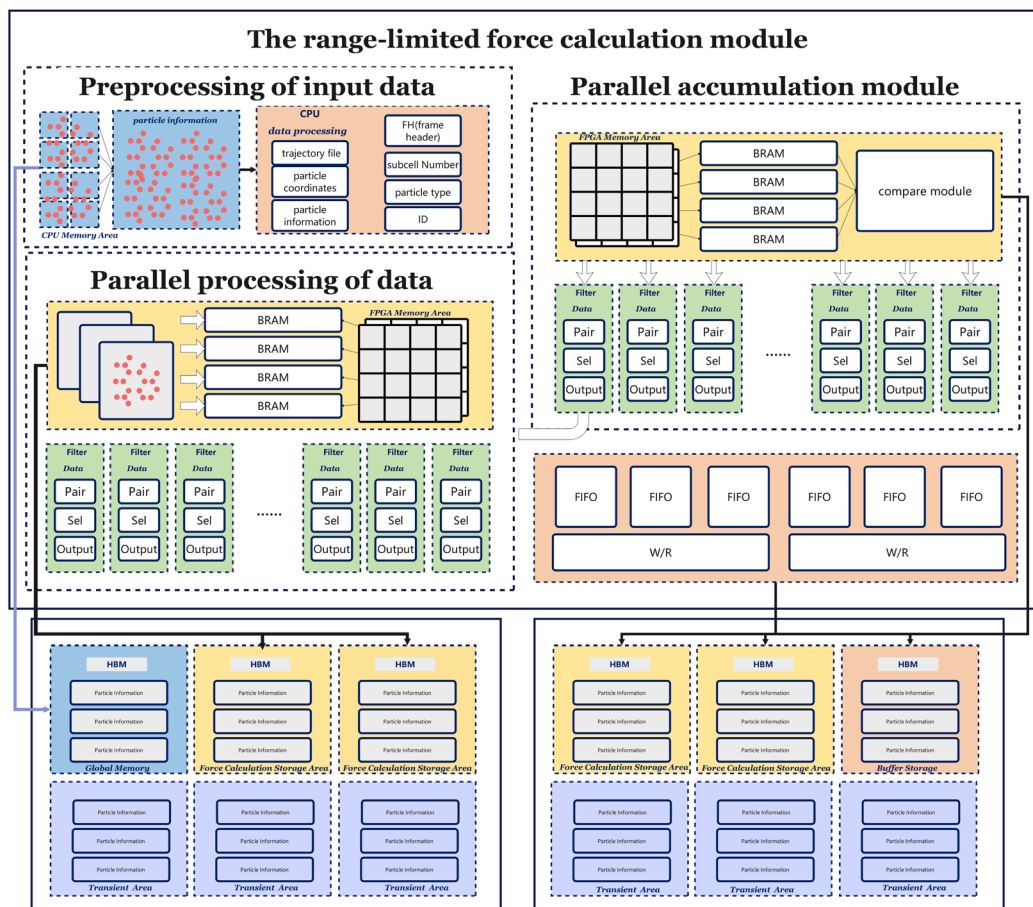


Fig. 1 Architecture of the range-limited force calculation module implemented on an FPGA acceleration card. Key components include: preprocessing of input data (CPU), a neighbor-list generator with cutoff-radius filtering, parallel force-computation pipelines (data module shown), a parallel accumulation network, and a PCIe host interface with a DMA engine. The dataflow follows MD requirements with double-buffered position updates and pipelined force accumulation.

through the cell serial number, and the length is allocated based on the maximum expected number of particles, with a margin reserved. An exclusion information table, containing bonded particle pairs, is also stored in the memory. This data table structure allows exclusion of the particle information in pairs, and the number and addresses of excluded particles are registered and accessed by the relevant modules during computation. The neighboring force calculation uses interpolation and coefficient tables, which are generated by the CPU and configured into the on-chip RAM of FPGA. After configuration, the CPU initiates prefetching of particle data units, and the parallel reading module supplies particle-pair information to the pipeline. Next, the multi-channel screening module processes each data unit as a main cell. It retrieves particle information from the main cell and its 13 neighboring cells to construct candidate particle pairs for distance evaluation. Specifically, each particle in the main cell is paired with particles from each of the 13 adjacent cells. The module filters out any pairs that exceed the cutoff distance. The half-shell cell-partitioning method proposed by Bowers *et al.* is adopted to reduce computational redundancy.⁴⁰ For those within the cutoff, interpolation coefficients are computed based on

squared inter-particle distances and type information. These coefficients, along with charge data, are used to evaluate electrostatic and short-range forces. All parameters required for the RL force calculation are stored in the FPGA's on-chip RAM and passed to the distance-judgment module, ensuring that only relevant pairs proceed to the next computation stage. The range-limited force-calculation module monitors this process, updating the force-calculation result data table and overseeing the calculation progress.

3.2 Data reading and writing with HBM memory

HBM2 stores data units in a structured manner, with each unit containing multiple layers of information.^{34,41} The main row encodes essential metadata, including the cell serial number, particle charge, storage offset address of the particle information, and parity bits. This metadata provides the foundation for subsequent data processing. Subsequently, each quadrant uses the serialized identifier and the HBM address offset of the adjacent units to record the adjacency relationship in an orderly manner.



Each spatial dimension is stored in a continuous 8-byte block, making data associations clearly traceable. Memory allocation follows a strict alignment protocol. For incomplete rows, padding is carried out to meet the requirements of the complete row boundary. Particle-specific serial numbers are stored sequentially in continuous memory segments, and the established alignment rules are maintained through terminal padding to ensure the standardization of data storage. Such a hierarchical layout not only ensures the integrity of the memory architecture but also enables efficient data access and retrieval. In contrast to the ring-based communication scheme proposed by Wu *et al.*⁴² for managing fan-in/fan-out during particle pairing, our design leverages HBM2's multi-channel parallelism and address interleaving to achieve high-throughput access without explicit ring communication, thereby simplifying data movement while maintaining scalability. During caching, multiple channels can simultaneously read data, either at the same address or different addresses, as detailed in SI Fig. S3.

3.2.1 Data structure of the particle table: HomeCell and NeighborCell. Each data unit adopts a specialized row-allocation strategy to accommodate a single particle. During the preprocessing stage, the size of each data unit is determined by estimating the maximum expected number of particles, with a safety margin applied. A hierarchical addressing mechanism allows direct access to any data unit *via* its unique serial number, which maps to a precise memory location.

Structural omissions are made for particle items, resulting in a specialized memory topology. This layout is elaborated in detail in Fig. S3, serving as a reference structure for the computation modules of the 13 adjacent cells. The calculation of non-bonding forces uses the pre-computed interpolation coefficients and lookup tables that are loaded in the dedicated on-chip RAM resources. For particle pairs that do not require explicit calculation, identifiers of excluded bonded pairs are stored in shared memory as particle ID pairs. This arrangement ensures low-latency access during force calculations.

The particle information storage architecture establishes a dual-layer hierarchy between HomeCell and NeighborCell structures operating on 512-bit data buses, where non-functional regions undergo zero-padding optimization to maintain address alignment and facilitate efficient lookup operations as shown in Fig. 2 and 3. This unified storage schema consists of seven functional segments defined by fixed bit allocations. The initial segment uses a lookup code for rapid classification, directing processing pipelines to the appropriate computation modules based on the encoded metadata. Serial numbers are assigned globally to ensure unique identification of all simulation entities. Spatial coordinates embed precise 3D positions in the Cartesian coordinate system. Particle identifiers follow a global numbering scheme, enabling consistent tracking across the simulation. The architecture employs a hybrid addressing paradigm, combining hierarchical indexing of cell relationships with direct particle access. Register-mapped exclusion tables dynamically configure FPGA resources for force calculations.

This structured approach ensures deterministic memory-access latency while maintaining compatibility with parallel processing architectures.

3.2.2 Data structure of the HomeCell. The particle information repository adopts a fixed-length encoding scheme within 512-bit HomeCell structures, maintaining alignment constraints through zero-padding strategies that enhance address-resolution efficiency (Fig. 4). This standardized format segments data into five predefined fields with dedicated bit allocations, beginning with a machine-readable type identifier that directs processing workflows to the designated arithmetic units. Each particle's physical attributes, including partial charges (scalar), velocities (vector), and coordinates (vector), are encoded using IEEE 754-compliant 32-bit floating-point representations to ensure numerical stability.⁴³

To support parallel processing, a dual-tier memory management strategy is employed: precomputed pairwise interaction data for the first 13 nearest NeighborCells are stored in on-chip registers for immediate access, while data for the remaining 13 neighbor cells are staged in 256-bit wide global memory buffers (Fig. 3). This partitioning balances latency-sensitive intra-cell computations with bandwidth-intensive inter-cell calculations and is supported by FPGA-optimized neighbor-index register files that reduce off-chip memory access. Again, the storage architecture is designed to simultaneously satisfy deterministic timing constraints for core physics kernels and maintain data-handling capacity for large-scale particle systems.

3.2.3 On-chip force accumulation between HomeCell and 13 NeighborCells. The particle-to-force caching and partial summation module implements a latency-optimized data-reuse scheme by sequentially capturing force-calculation results between a primary cell's particle and its intra-cell counterparts across successive clock cycles. This approach consolidates redundant force components into interim storage buffers, substantially reducing data movement while preserving computational consistency. Central to this mechanism is a hierarchical aggregation logic that associates force contributions with their source particles *via* unique serial-number indexing, enabling parallel accumulation of vector forces within dedicated on-chip registers. The resulting composite force vectors are then serialized into contiguous memory locations based on source-particle identifiers, forming structured force caches aligned with downstream processing requirements.

The range-limited force buffer adopts a linear addressing scheme in which entries align directly with particle enumeration, ensuring deterministic memory-access patterns essential for maintaining synchronization during large-scale *N*-body simulations. This structured methodology simultaneously minimizes off-chip bandwidth consumption and maximizes FPGA resource utilization through optimized register-file data structures.

3.2.4 Memory management and layout for NeighborCells. During particle computation, a unified hierarchical storage architecture is employed for data caching. Its 512-bit data frame structure, shown in Fig. 3, comprises two functional rows: the



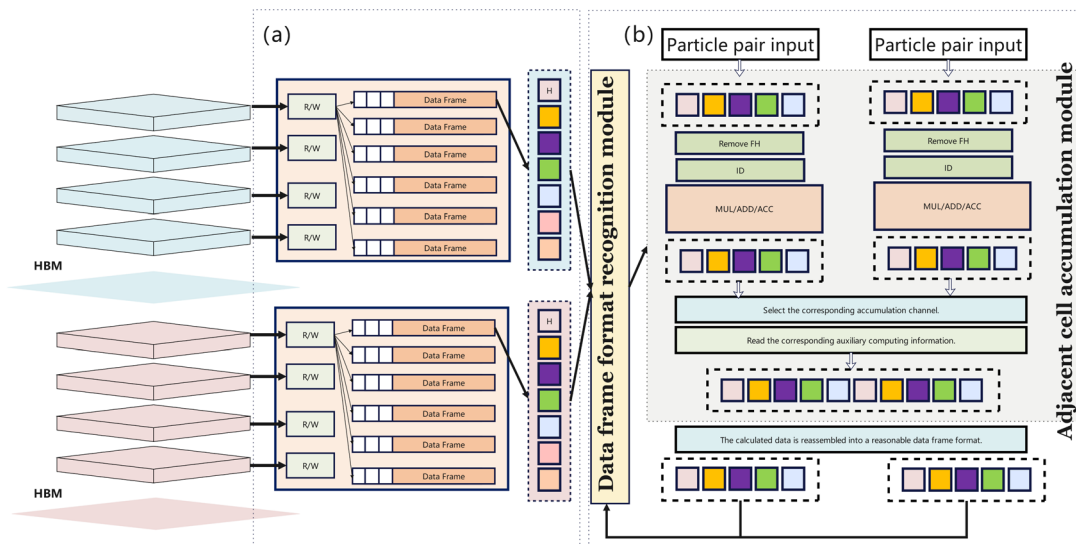


Fig. 2 Particle data processing system architecture. (a) HBM-based data storage structure. The architecture employs dual HBM stacks, with each stack configured with 3 channels (as illustrated). Twelve independent read/write controllers (distributed as 4 per HBM stack) manage data flow, featuring 128-bit-wide data frame buffers and HomeCell markers (denoted by red/blue H-tags). Data organization follows an interleaved memory access pattern, with frame-level parity checking implemented (though not visually depicted). (b) Computational pipeline. The input stage comprises (i) particle-pair filtering via the “Remove F” block, (ii) ID validation (green “ID” module), (iii) parallel multiply-accumulate units (purple “Mul/Add” blocks), and (iv) dynamic channel selection governed by the orange multiplexers. The output stage handles data-frame reassembly (rightmost green module) and synchronizes adjacent accumulators through the “Adjacent Conv. Uni.” linkages (indicated by arrows).

index row and the data row. The index row encodes key operational parameters, setting fields such as the type-classification flag and particle identifier through designated bits. Among these, the buffer capacity is predefined as twice the maximum number of particles observed during preprocessing. The valid

entry counter is initially set to zero, and a 16-byte segment checksum is included for error detection.

Buffer management follows a two-stage protocol to handle data insertion and calculation. The dynamic memory offset is determined according to the valid-entry count. The counter is

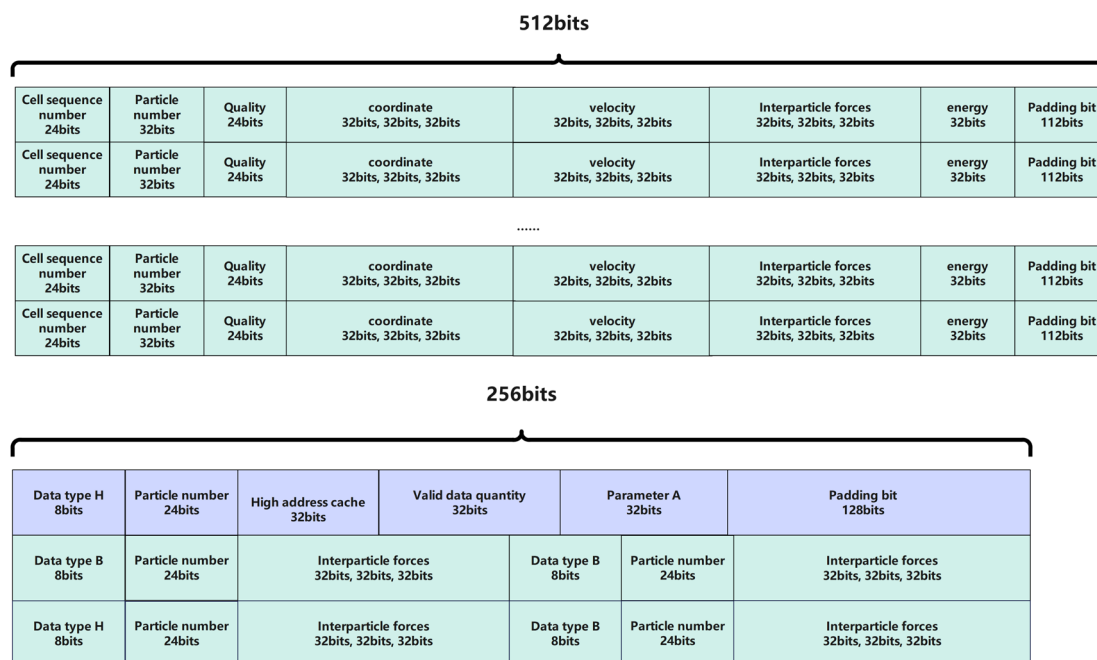


Fig. 3 Block diagram of the storage structure of the RL force-result buffer. The calculation result of each particle pair is stored as 256-bit data. Each step’s result is written to a designated storage space and later processed by the CPU for the remaining calculations.



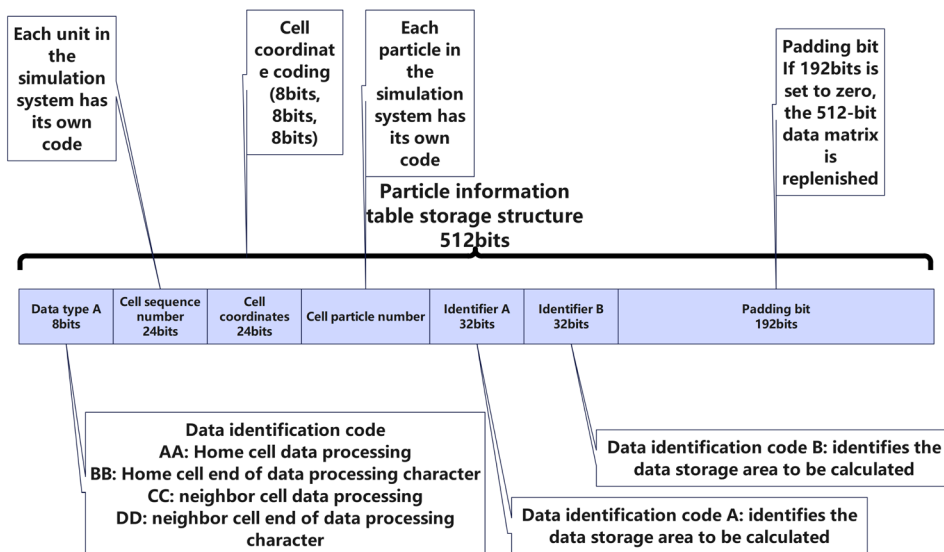


Fig. 4 Storage structure of HomeCell and NeighborCells in the particle table: 512-bit data composed of six parts.

incremented after each write operation, and at the same time, the checksum for the first 16 bytes of the index row is regenerated. The dual-buffer design endows the system with the ability to resist overflow during peak calculation cycles. The IEEE 754 single-precision floating-point format is adopted to process the velocity, position, and charge components, ensuring numerical stability in the parallel processing pipeline. Compatibility with the FPGA-based DMA engine is maintained to enhance data transfer efficiency from the host to the device.

3.3 Range-limited force calculation

3.3.1 Interpolation table setup. As shown in Fig. 5, the range-limited force calculation assumes that particle i and

particle j have already passed through the particle-pair screening module. Only particle pairs that meet predefined criteria (*e.g.*, within the cutoff distance) are processed through the DSP-based direct calculation pipeline for efficient force computation. This approach achieves higher numerical accuracy than fixed-point or reduced-precision alternatives. However, FP32 arithmetic consumes more DSP resources than integer or lower-precision operations,⁴⁴ imposing a trade-off between precision and computational efficiency. In existing studies, interpolation lookup tables have been used to replace traditional direct calculation methods, thereby saving resources.^{33,45,46} The force-interpolation strategy proposed by Chiu *et al.* has been extended to HBM2-based architectures for larger systems.⁴⁷

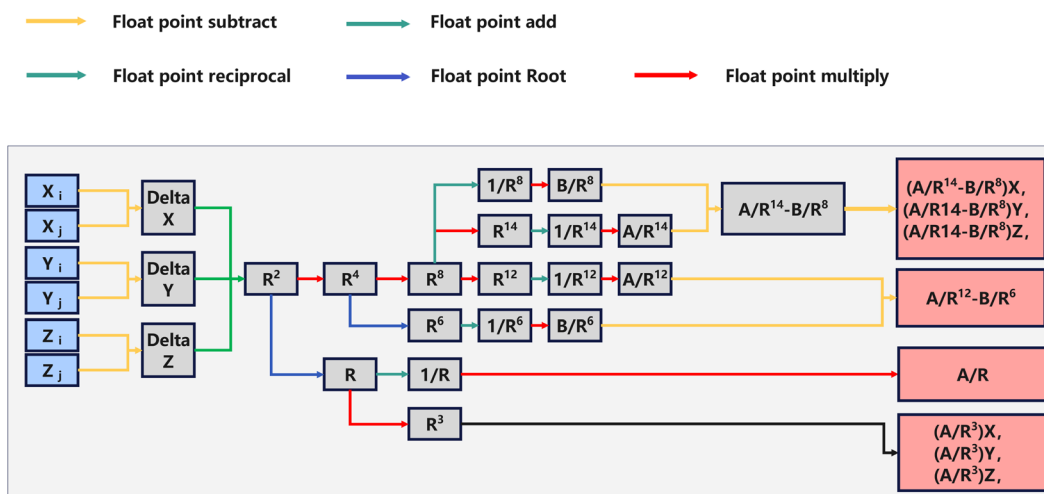


Fig. 5 Block diagram of the direct calculation module, assuming that particle i and particle j have gone through the particle screening module and their short-range interaction needs to be computed within a specified cutoff range. The force between the particle pair is calculated directly by the DSP pipeline using single-precision floating-point arithmetic, implemented *via* the Xilinx floating-point unit. This method offers relatively high precision but consumes a significant amount of DSP resources.



$$F^{\text{RL}} = A_{\text{ab}}r_{ij}^{-13} + B_{\text{ab}}r_{ij}^{-7} + Q_{\text{ab}}r_{ij}^{-2} \\ = r_{ij} \times (A_{\text{ab}}r_{ij}^{-14} + B_{\text{ab}}r_{ij}^{-8} + Q_{\text{ab}}r_{ij}^{-3}), \quad (11)$$

where

$$A_{\text{ab}} = 48\varepsilon_{\text{ab}}\sigma_{\text{ab}}^{12}, \quad (12)$$

$$B_{\text{ab}} = -12\varepsilon_{\text{ab}}\sigma_{\text{ab}}^6, \quad (13)$$

$$Q_{\text{ab}} = \frac{q^a q^b}{4\pi\varepsilon}. \quad (14)$$

In this design, r_{ij}^{-14} , r_{ij}^{-8} and r_{ij}^{-3} are required for the range-limited force computation. To reduce DSP usage, r_{ij}^2 is taken as the fundamental variable, and interpolation functions for these inverse powers are precomputed. Each target function is reduced to a low-order monic polynomial in r_{ij}^2 , enabling reconstruction of the original values while simplifying arithmetic and lowering resource consumption. The interpolation functions are designed to balance reduced computational complexity with sufficient numerical accuracy. The performance of first-, second-, and third-order interpolation schemes was compared. By selecting an appropriate sampling interval, the derivatives of the target functions can be numerically approximated at discrete points, allowing polynomial fits valid over the chosen range. In our implementation, the second-order interpolation scheme divides the interval [0.1, 144] into eight primary segments: [0.1, 0.2], [0.2, 0.4], [0.4, 0.8], [0.8, 1.6], [1.6, 3.2], [3.2, 6.4], [6.4, 16.0], and [16, 144]. The first 7 segments are each further divided into 16 subsegments, while the last segment is split into 128 subsegments, yielding 240 interpolation functions in total. Each interpolation function requires 3 single-precision floating-point coefficients, and the full interpolation table fits within a 4 KB BRAM.

The range-limited force calculation also requires coefficient tables for A_{ab} and B_{ab} , where each particle-type pair has a unique set of coefficients. For N particle types, the coefficient table length is N^2 . The current design supports up to 32 distinct particle types, resulting in a maximum table depth of 1024 entries, sufficient for most MD systems.

In hardware floating-point computation, root operations are costly in logic resources. Therefore, r_{ij}^{14} and r_{ij}^8 are computed *via* repeated multiplication from r_{ij}^2 , avoiding explicit square-root operations. A separate lookup table handles Coulomb forces. Parallel computations operate independently, with final results generated after floating-point multiplication and division, combined with particle parameters (A_{ab} , B_{ab} , *etc.*) fetched from memory, as illustrated in Fig. 6. Since these parameters remain constant during a simulation, the particle-pair lookup table can be precomputed, further reducing calculation logic and runtime.

3.3.2 Computation control modules. The particle computation control framework integrates multiple functional layers to oversee and optimize neighbor identification and force aggregation pipelines. As shown in Fig. 7, a hierarchical memory architecture manages cell metadata through dynamic matrix structures. A 2D array (module a) scales with system-wide

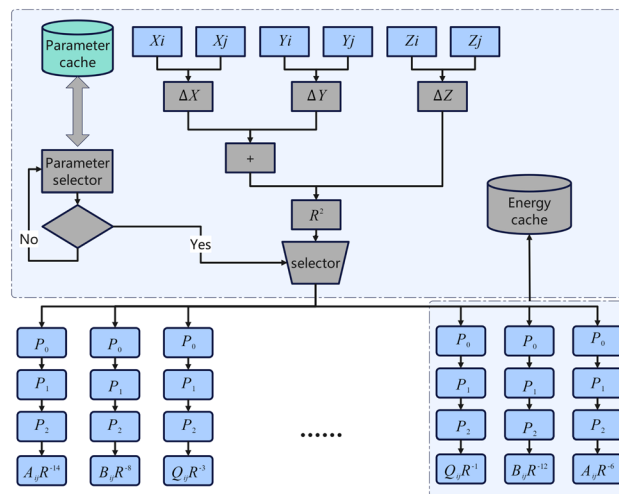


Fig. 6 Framework diagram of the DSP processing flow for second-order interpolation tables. Particle information is first read from the parameter cache. After arbitration by the parameter selector, particle pairs undergo distance evaluation. Pairs within the interaction range are routed to the force computation channel, assuming that the particles to be computed are particle i and particle j .

cell populations to track neighbor indices per home cell, while a 1D auxiliary array (module b) supports rapid index comparison and cross-referencing operations. A parallel comparison engine (module c) evaluates eligibility criteria across these matrices using hardware-accelerated voting logic, enabling deterministic selection of interacting home cells based on spatial-proximity thresholds.

Sequence control is managed through a stateful counter array (module d) that enforces strict access patterns to prevent memory-coherence violations. Data retrieval from external HBM is coordinated by a pipelined fetch unit (module e), which retrieves composite particle-attribute blocks—each home cell requires 13 cumulative data segments including self and 12 neighbor cells through burst-optimized HBM controllers. The external storage subsystem (module g) employs bank-interleaved addressing to resolve latency bottlenecks arising from concurrent access requests, while a data-fusion module (module f) aggregates force vectors from intra-cell and inter-cell interactions using SIMD-aligned accumulation registers. This architecture achieves sub-microsecond neighbor-search latencies through optimized matrix compression and pipelined dataflow.

3.4 FPGA implementation of PME for long-range electrostatics

For PME calculations of electrostatic interactions, we implemented a computationally intensive three-dimensional (3D) Fast Fourier Transform (FFT) module on FPGA, while delegating the remaining computational tasks to CPUs.^{29,48,49} Data exchange between the CPU and FPGA is facilitated through high-speed PCIe interfaces or optical fiber connections.⁵⁰ To accelerate the calculations, we also developed a parallelized approach that leverages proximity lookup tables for Ewald



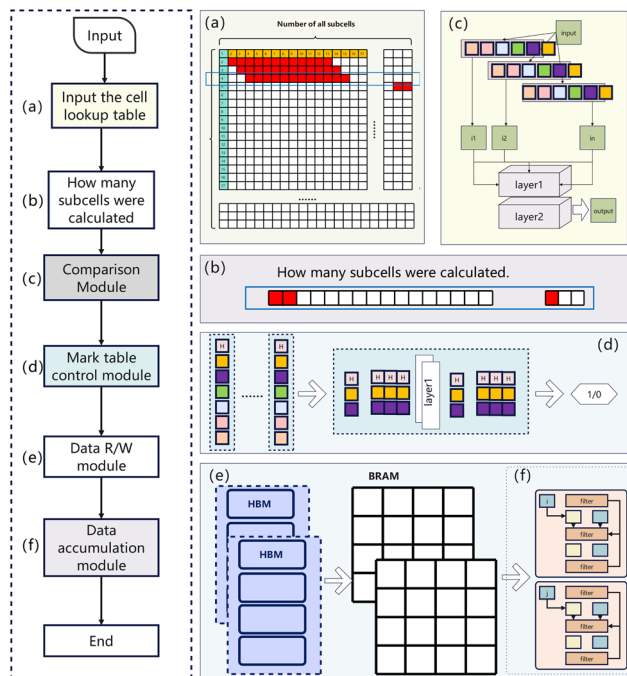


Fig. 7 Architecture of the particle computation progress-monitoring module. (Left) Computational workflow: Input layer: receives cell lookup table (2D array) and progress tracking data (1D array). Comparison module: verifies completion status of 26 Neighbor-Cell interactions per Home Cell. Marktable control: flags completed calculations using bitmask (1/0). Data R/W module: coordinates HBM access for parameter retrieval (3-channel HBM interface shown). Accumulation module: filters and aggregates intermediate results through parallel pipelines. (Right) Data structures and hardware implementation: (a) 2D Neighbor index array: memory block indices for 26 neighboring cells (17×26 matrix shown). (b) 1D Progress tracker: calculation state vector for Home Cells (17-element array). (c) Hierarchical comparator: 3-layer logic verifying neighbor-cell completion (input \rightarrow layer1 \rightarrow layer2 \rightarrow output). (d) Bitmask generation: converts comparison results to completion flags (boolean layer2 output). (e) HBM interface: triple-channel memory controller with address translation logic. (f) Result accumulation: three-stage filtering for force/energy summation (FP32 precision).

summation, achieving a level of parallelism comparable to that of vdW force calculations.⁵¹ The simulation box is partitioned into cubic or rectangular grids along the X , Y , and Z axes, with grid dimensions determined by the system boundaries to optimize data alignment and hardware tiling.

Charge assignment to grid points is performed using third-order B-spline interpolation. Temporal-spatial domain transformations are carried out using optimized FFT algorithms for frequency-domain computations. The hardware implementation builds upon OpenMM's reference codebase,⁵² with kernel-level optimizations achieving up to a 15 times speedup in Coulomb force calculations compared to CPU-only implementations when tested on the Inspur F37X platform. Resource utilization analysis reveals 83% DSP block efficiency and 72% HBM2 bandwidth saturation when simulating a solvated protein system of approximately 100 000 atoms, demonstrating the feasibility of this design for large-scale MD workloads.

The 3D FFT calculation proceeds sequentially along each axis (X to Y to Z), where the output of each dimension serves as the input for the next. The architectural design of this multi-stage transformation is shown in Fig. 8. Once the Z -dimension FFT is completed, the convolution module retrieves coefficients from local memory and performs convolution; for the X and Y dimensions, convolution is skipped. The processed results are then passed to the data conversion module for further handling. To improve FFT performance, we adopted the FFT 9.0 IP core.⁵³ Among its available modes, the pipelined configuration provides the highest throughput, albeit with increased resource consumption. Performance measurements for this configuration are reported in Table 1.

The $64 \times 64 \times 64$ FFT computation exhibits near-linear scaling compared to the $32 \times 32 \times 32$ case, requiring approximately $8\times$ the time—consistent with the $\mathcal{O}(N^3 \log N)$ complexity of 3D FFTs. This aligns with theoretical expectations, as doubling each dimension (X , Y , Z) increases total points by $8\times$, while the logarithmic term accounts for the FFT's hierarchical decomposition stages.⁵³ Performance metrics of Anton1, though groundbreaking for its era, are now outpaced by contemporary FFT implementations. For instance, Anton3's specialized MD simulation architecture demonstrates $100\times$ faster throughput than generic supercomputers,²³ suggesting similar leaps in FFT efficiency through domain-specific optimizations (e.g., reduced data movement and compressed encoding).

3.5 Calculation pipeline of bonded forces

Fig. 9 illustrates the cooperation mode between CPU and FPGA in the calculation of bonded forces, with data transmission between software and hardware realized through PCIe.⁵⁴ Each small box in the diagram represents a circuit processing unit. The bonded forces include the bond, angle and dihedral terms in the classical FF models. In MD simulations with classical FFs, the topology, which defines how particles are connected with covalent bonds, remains fixed throughout the simulation. Particle and topology information is obtained from user input files, and the structure of the particle-information storage table can adapt to the specific topology inputs. This data is stored in a specific cache area of HBM2 using DMA technology. The FPGA data read/write submodule employs multiple channels in parallel, and is equipped with HBM2 registers, which can support multiple read and write operations simultaneously. This allows the system to efficiently read interaction data for two-body (bond), three-body (angle), and four-body (dihedral) bonded terms. The design significantly improves storage and access efficiency for large data blocks.

The computation flow-control circuit manages the bonded-force calculations. Two-body force calculations are relatively straightforward and thus execute more quickly. Three-body force calculations are moderately more complex and slower, while four-body force calculations are the most computationally intensive, both in processing time and complexity, making them the primary bottleneck in the bonded-force pipeline. The covalent-bond calculation buffer is designed with these



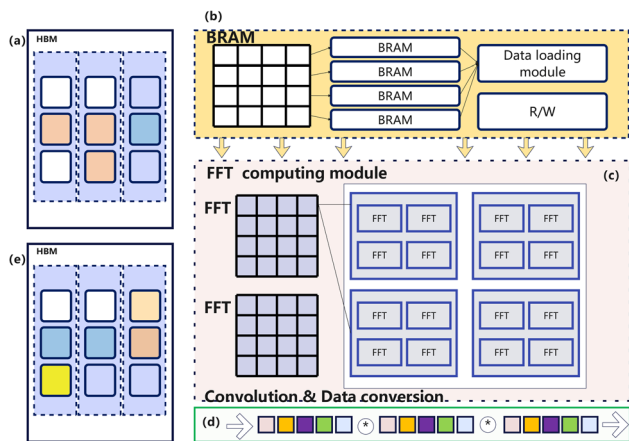


Fig. 8 3D FFT acceleration module architecture. (a) Dual HBM memory banks (left/right) with interleaved data blocks (white/orange/blue/yellow) and virtual channel interfaces. (b) Central BRAM interface layer containing 8 BRAM modules (4 KB each), data-loading module (512-bit bus), and R/W controller with arbitration logic. (c) Parallel FFT processing array with 16/32 FFT units (4 clusters of 4 units each) implementing Radix-4 butterfly networks at 300 MHz. (d) Bottom-stage convolution and data-conversion pipeline performing 6-step mixed-precision processing (FP32 to INT8). (e) Complete data flow path: HBM memory to BRAM cache to FFT array to convolution module and back to HBM.

Table 1 Implementation of 3D FFT computation module using Xilinx Virtex UltraScale+ VU37P accelerator card. The module completes data reading, 3D FFT computation, convolution, inverse transform, and data storage. Pipelined mode is configured for testing. Input data includes single-precision floating-point matrices of dimensions 32×32 and $64 \times 64 \times 64$

Model	Clock frequency	32 × 32 (μs)		64 × 64 (μs)	
		32 × 32 (μs)	64 × 64 (μs)	32 × 32 (μs)	64 × 64 (μs)
FPGA VU37P	300 MHz	18.33	119.7		
NVIDIA ⁵³ Tesla K20c	0.73 GHz	29	92		
Anton ²¹		4	13		

differences in mind: it incorporates specialized circuits to receive data from channels with varying access frequencies, ensuring efficient handling across all bonded-interaction types.

3.6 Performance and resource utilization of computing modules

3.6.1 Performance of the particle-pair computation module designed via HLS. This study explores FPGA-based acceleration for MD simulations, focusing on non-bonded-force calculations through heterogeneous computing. In the hardware implementation of the range-limited module, a hybrid design strategy is employed to balance low-latency requirements with resource efficiency. Multi-order interpolation units (1st, 2nd, and 3rd order) are implemented in Vivado HLS, exhibiting near-linear scaling in both resource usage (10/16/22 DSP48) and latency (22/34/45 cycles at 300 MHz). In addition to DSP slices, the two other major FPGA resources—Look-Up Tables (LUTs) and Flip-Flops (FFs)—are also tracked,

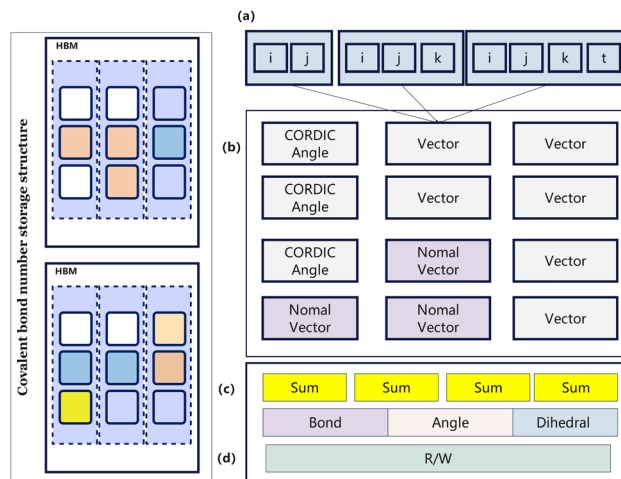


Fig. 9 Covalent bond force computation architecture with reusable logic. The left panel shows two HBM memory banks for covalent-bond-number storage, each organized into three vertically stacked sections with color-coded blocks (white, orange, light blue, and yellow) representing different bond-parameter sets. The right panel illustrates the computational pipeline: (a) The top section contains three index arrays labeled "ij", "ijk", and "ijkt" for 2-body, 3-body and 4-body interactions, respectively. (b) The middle section features six parallel vector computation modules feeding into three normal-vector generators. (c) The lower section implements four summation units (yellow) that aggregate results for bond, angle and dihedral terms. (d) The bottom green module handles final read/write operations.

with their utilization summarized in Table 2. The HLS results deviate by less than 15% from manually optimized Verilog RTL, supporting the use of HLS for algorithmic components. Rather than instantiating HLS IP cores directly, we further optimize the generated Verilog to enable finer resource control, including DSP48 reuse and pipeline-depth tuning.

On the device, the RL unit occupies only 12–18% of the total module area. A modular AXI interface enables seamless integration with the predominantly RTL design. This hierarchical approach preserves RTL's cycle-accurate control over critical paths while leveraging HLS for rapid development of compute-intensive functions. The standardized AXI4 protocol not only decouples submodules but also establishes a scalable foundation for future multi-module chaining through configurable address mapping and clock domain crossing support.

The HLS implementation demonstrates efficient resource utilization in specific operations, such as second-order polynomial interpolation (10 DSP48 modules at 300 MHz and 22-cycle latency) and r_{ij} distance calculation (9 DSP48 and 25 cycles). In contrast, RTL-designed modules show greater potential for latency optimization of certain operations. For example, the bonded-force module designed with RTL achieves balanced resource usage (15% LUTs and 14% FFs) with only 3% DSP occupation. RTL design also allows on-chip memory balance by distributing data across LUTs, Block RAM (BRAM), and UltraRAM (URAM); in particular, URAM-based designs reduce BRAM consumption by 58% through refined memory architectures. Essentially, we adopt a hybrid approach that leverages HLS for rapid prototyping of coarse-grained



Table 2 Performance and resource evaluation of multiplication and addition of first-order polynomials using Xilinx's HLS, totaling 10 DSP48 modules. With a clock constraint of 300 MHz, Pipeline requires 22 clock cycles to complete the functional implementation. The performance and resource evaluation of multiply-add second-order polynomials using Xilinx's HLS is performed on a total of 16 DSP48 modules. The pipeline requires 34 clock cycles to complete the functional implementation; Xilinx's HLS is used to evaluate the performance and resources of the multiply-add operation for third-order polynomials, totaling 22 DSP48 modules. With a clock constraint of 300 MHz, the pipeline requires 45 clock cycles to complete the function

Modules	Latency		Resources		
	Cycles	ns	DSP	FF	LUT
First-order linear interpolation	22	73.304	10	1459	763
Second-order linear interpolation	34	113.288	16	1788	1063
Third-order linear interpolation	45	148.514	22	2442	1452

parallelism while reserving RTL for latency-critical components. Experimental results confirm RTL's consistent cycle-level advantage (*e.g.*, 34-cycle Coulomb force *vs.* 45-cycle HLS interpolation), albeit at the cost of more extensive development effort. Overall, these findings underscore RTL's adaptability for applications requiring sub-nanosecond precision, while also motivating further exploration of HLS-RTL co-design strategies.

3.6.2 Resource utilization and scalability of the range-limited force module. Table 3 reports the hardware resource utilization for loading a single RL force module and a dual-module configuration on the Xilinx Virtex UltraScale+ VU37P. In the baseline case of a single RL module, a modest fraction of the available resources is used: 10% of LUTs, 13.13% of FFs, 17% of GTs, and 7% of BRAM. This relatively lightweight footprint highlights the efficiency of the design and leaves substantial room for additional modules or auxiliary compute units. The balanced use of compute and memory resources also indicates that the single-module implementation is well suited for integration into larger heterogeneous systems. Importantly,

Table 3 Comparison of resource utilization between a single RL module and two RL modules in a finite range on Xilinx Virtex UltraScale+ VU37P with Inspur F37X

Resource name	Utilization%	
	Single RL module	Double RL modules
LUT	10	21
LUTRAM	3	6
FF	13.13	26.4
BRAM	7	18.5
URAM	0.63	—
DSP	2	4
IO	1	1
GT	17	34
BUFG	3	6
MMCM	8	16
PLL	17	34

the finer-grained pipeline control provided by RTL-based design enables near-linear resource scaling across multiple modules and allows cycle-level adjustments for ultra-low-latency operation.

Expanding to two RL modules demonstrates the scalability of the architecture. Resource usage increases in a near-linear manner—LUTs rise to 21%, FFs to 26.4%, and GTs to 34%—showing that both computational and communication demands scale proportionally with the number of modules. BRAM utilization also grows from 7% to 18.5%, while URAM becomes unused, suggesting a deliberate memory-hierarchy strategy that prioritizes BRAM capacity over URAM bandwidth in multi-module deployments. This consistent scaling behavior underscores the inherently parallel nature of the design and its suitability for deployment in larger compute matrices, where dozens or hundreds of RL modules could operate concurrently with predictable performance and resource characteristics.

3.6.3 Resource utilization of the long-range Coulomb force and the bonded-force modules. Table 4 reports the hardware resource utilization of the long-range Coulomb force module, implemented with the Xilinx FFT 9.0 IP.⁵⁰ On the same FPGA platform, adopting a URAM-based memory design significantly alleviates BRAM requirement, reducing BRAM usage from 58% to 24% while introducing a moderate 16% URAM occupation. This shift establishes a more balanced memory hierarchy compared with BRAM-centric designs.

Logic resources (LUTs, FFs, DSPs) and I/O components (GTs, PCIe) remain modestly utilized in the range of 14–17%, leaving ample headroom for additional computational workloads despite the high resource demand of FFT operations. Nonetheless, deploying multiple FFT IPs in a single-node setup requires careful trade-off analysis, as their substantial memory and compute requirements may compete with residual BRAM (24%) and other module allocations, necessitating holistic resource optimization. We note that for the full PME pipelines, FFT modules must coexist with range-limited and bonded-force modules.

Table 4 Layout routing uses Xilinx Virtex UltraScale+ VU37P chip. The utilization based on URAM uses resources more evenly compared with that based on BRAM

Resource name	Utilization%	
	Based on BRAM	Based on URAM
LUT	16	15
LUTRAM	4	4
FF	14	14
BRAM	58	24
URAM	—	16
DSP	7	7
IO	1	1
GT	17	17
BUFG	2	2
MMCM	8	8
PCIe	17	17



The bonded-force module, in contrast, is relatively lightweight and can be integrated efficiently into the overall design. As shown in Table S2, it demonstrates a well-balanced resource utilization on the Xilinx Virtex UltraScale+ VU37P platform. LUTs and FFs are occupied at 15% and 14%, while BRAM and URAM usages reach 24% and 13%, respectively. DSP usage is low (3%), and clock management resources (BUFG/MMCM) remain modest at 2% and 8%.

3.7 Validation: energies and forces of LJ particles

Validation of MD implementations typically involves verifying that the energies and forces are computed correctly. We applied this principle to our FPGA-based implementation of MD simulations with classical FFs. As an initial check, we considered a simple system: two LJ particles interacting with parameters $\sigma = 3.0 \text{ \AA}$ and $\epsilon = 2.092 \text{ kJ mol}^{-1}$ under periodic boundary conditions. We compared our implementation with CPU and GPU versions of OpenMM. Specifically, CPU-based reference results were obtained using an Intel i5-8400 (2.80 GHz) with OpenMM version 6.0.0, selected for its transparent implementation of 3D Fourier transforms;^{52,55} results were cross-checked against version 8.0 to confirm consistency. The code was compiled with the GNU C/C++ compiler 13.3.0. GPU-based results were generated on an NVIDIA GeForce GTX 1650 (driver 550.120, CUDA 12.4) using mixed-precision computation. Unless otherwise noted, subsequent benchmarks follow these same hardware and software configurations.

We computed both the total energy and the force on one of the particles (symmetry makes evaluation of a single particle sufficient). The test system was placed in a 30 \AA periodic box with a cutoff distance of 15 \AA , and inter-particle separations ranging from 2 to 28 \AA were sampled. As shown in Fig. 10, the system energy profile is symmetric about 15 \AA , consistent with

PBC applied. Beyond the cutoff distance, forces behave as expected, with each particle effectively interacting with the periodic image of the other across the box boundary. A further inspection between 2.5 to 8 \AA further confirms that the FPGA implementation closely matches the CPU and GPU results (Fig. 10c and d). The FPGA-calculated energy exhibits a root mean square error of $1.5 \times 10^{-5} \text{ kJ mol}^{-1}$ compared to the OpenMM CPU results, demonstrating numerical equivalence. These results validate that our implementation—particularly the range-limited force module—accurately reproduces LJ interactions on FPGA hardware.

To further evaluate accuracy with more complicated systems, we extended the validation to a 15-atom argon cluster simulated in a 30 \AA cubic box with PBC. Parameters from the CHARMM force field ($\sigma = 3.8220 \text{ \AA}$, $\epsilon = 0.9961 \text{ kJ mol}^{-1}$) were employed with a 12 \AA cutoff for non-bonded interactions. Five distinct configurations were extracted from the MD trajectories, and the total potential energies were compared on FPGA, GPU, and CPU platforms as described previously. The LJ potential energies (Table S3) reveal very minor inter-platform deviations, confirming the accuracy of FPGA implementation. This cross-platform agreement demonstrates that our FPGA architecture achieves high computational precision in handling LJ interactions through parallelized execution and optimized memory-bandwidth utilization.

3.8 Validation: DHFR in explicit solvent

A further validation of our design and implementation involved MD simulations of a protein solvated in an explicit water box under PBC. We chose the DHFR system, a widely used benchmark in MD studies, consisting of 159 amino acids modeled with the AMBER ff99SB protein FF⁵⁶ and 7023 TIP3P water molecules, yielding a total of 23 558 atoms in a cubic box of $62.230 \times 62.230 \times 62.230 \text{ \AA}^3$. A non-bonded cutoff of 9 \AA was applied, PME was used for long-range electrostatics, and 50 000 steps were performed in the NPT ensemble with a time step of 2 fs at 300 K and 1.0 bar. Initial velocities were assigned randomly, and no additional heating or equilibrium was performed. Simulations were carried out in OpenMM on CPU and GPU (both in single-precision and double-precision). On the FPGA platform, our implementation supported full MD propagation, including all force calculations, as well as coordinate and velocity updates performed directly on the FPGA. An internal OpenMM interface was customized to enable output of the coordinates, velocities, or energies from the FPGA as needed, allowing direct comparison with CPU and GPU results.

The protein remained stable during 100 ps of MD simulation on FPGA, as shown in Fig. 11a, where the final snapshot from the FPGA trajectory was aligned with the initial structure. Although the simulation length is not sufficient to capture functionally relevant conformational dynamics, the heavy-atom RMSD profiles from FPGA and GPU simulations were highly similar, converging to 1.5 \AA after 100 ps (Fig. 11b). We note that different random initial velocities were assigned during validation across platforms, leading to variations in the observed properties at the beginning of the nonequilibrium stage, but

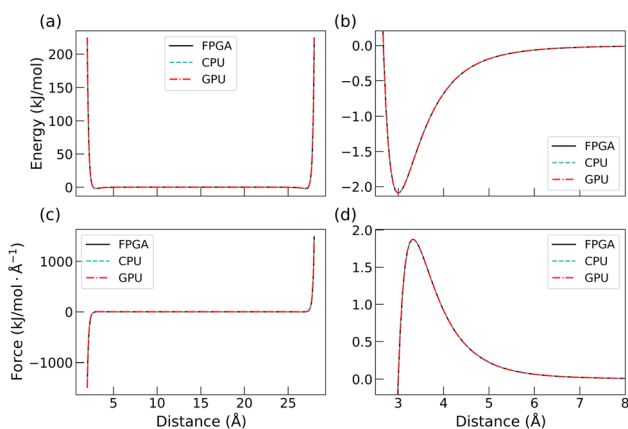


Fig. 10 Comparison of two-particle LJ system energy and single-particle forces as functions of inter-particle distance in a 30 \AA periodic box: (a) Total energy comparison between FPGA, GPU and CPU calculations. (b) Total energy comparison between FPGA, GPU and CPU calculations from 2.5 \AA to 8 \AA . (c) Single-particle force comparison between FPGA, GPU and CPU calculations. (d) Single-particle force comparison between FPGA, GPU and GPU calculations from 2.5 \AA to 8 \AA .



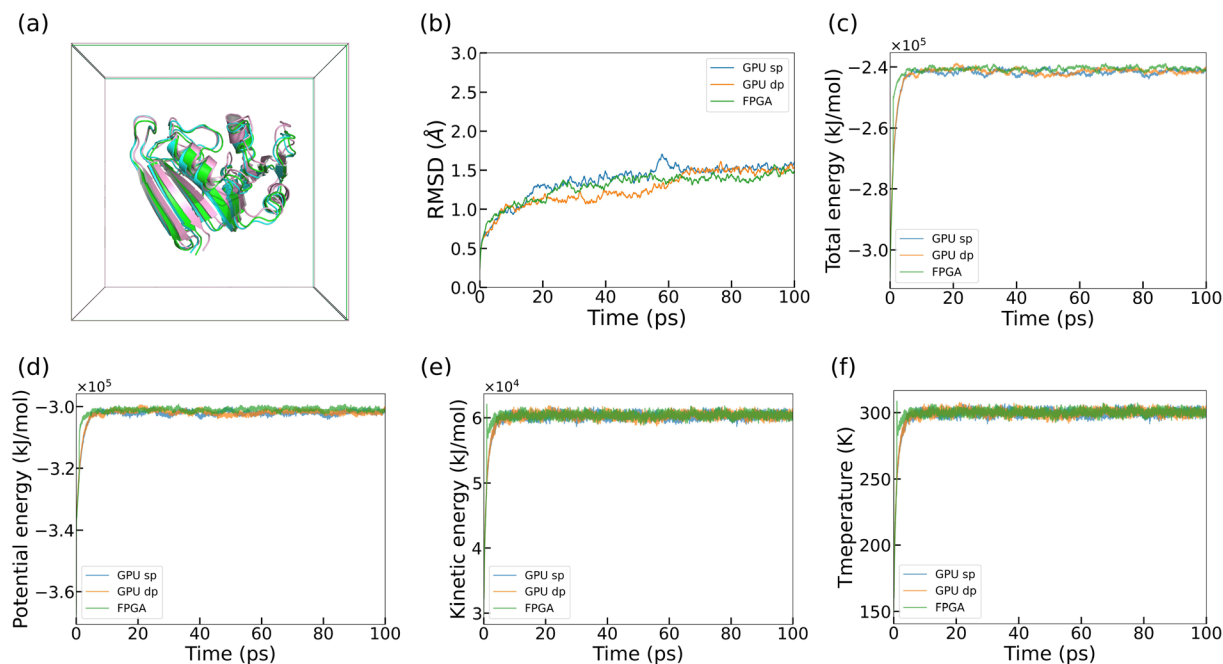


Fig. 11 Validation of MD implementation on FPGA employing the DHFR protein system compared with simulations performed on GPU. Simulations on GPU are performed with both single-precision (sp) and double-precision (dp) precision. (a) The final structures of DHFR after 100 ps simulation performed on GPU sp (green), GPU dp (cyan) and FPGA (pink), as well as the simulated box. (b) The RMSD evolution of DHFR heavy atoms over 100 ps. (c) The total energy of the simulated system in units of kJ mol^{-1} . (d) The potential energy of the simulated system in units of kJ mol^{-1} . (e) The kinetic energy of the simulated system in units of kJ mol^{-1} . (f) The temperature of the simulated system in units of K.

these quickly converge and fluctuate within the same reasonable range.

In addition, we compared the total, potential, and kinetic energies across platforms (Fig. 11). All energy profiles exhibited consistent trends and fluctuation ranges for FPGA, single-precision GPU, and double-precision GPU. The energies converged similarly within 200 steps. The last 80% of each trajectory was analyzed for average energies and fluctuations. The potential energy values were $-1\,263\,558.08 \pm 2574.67 \text{ kJ mol}^{-1}$ (single-precision GPU), $-1\,262\,739.74 \pm 2728.18 \text{ kJ mol}^{-1}$ (double-precision GPU), and $-1\,259\,214.13 \pm 2087.86 \text{ kJ mol}^{-1}$ (FPGA). The similarity in fluctuation ranges across platforms confirms proper energy conservation. Kinetic energy values were $252\,392.52 \pm 1666.11 \text{ kJ mol}^{-1}$ (single-precision GPU), $252\,512.85 \pm 1710.17 \text{ kJ mol}^{-1}$ (double-precision GPU), and $252\,723.81 \pm 1555.32 \text{ kJ mol}^{-1}$ (FPGA). These correspond to average temperatures of $299.92 \pm 1.98 \text{ K}$, $300.06 \pm 2.03 \text{ K}$, and $300.31 \pm 1.85 \text{ K}$, respectively. The observed fluctuations of 0.6% demonstrate robust temperature control across all cases, confirming that our FPGA implementation can perform MD simulations of realistic biomolecular systems with high precision.

While we demonstrated that MD simulation of a solvated protein is stable with our FPGA implementation, we further examined the accuracy by comparing the energies in detail. For this we extracted five snapshots along the MD trajectories and computed energy terms under the same hardware and software environments described above (Table 5). For all five snapshots, the total energies computed on FPGA showed excellent

agreement with GPU reference values, with the small deviations arising from the non-bonded-force terms. These differences most likely originated from electrostatic interactions, since the LJ terms had already been validated. The electrostatic discrepancies were traced to the 3D-FFT computation process, with two contributing factors: (1) the FPGA's native FFT IP core supports only power-of-two matrix dimensions (e.g., 32 or 64), and (2) the FFT v9.0 IP core provides both 32-bit floating-point and fixed-point modes, each with distinct resource utilization characteristics.

Despite these architectural constraints, our results confirm that the overall implementation is correct and produces physically meaningful outcomes. The observed deviations fall well within acceptable ranges for MD simulations and can be attributed to known hardware limitations. Taken together, these comprehensive results with a realistic protein system validate that our FPGA implementation is accurate and suitable for production runs. The achieved accuracy, combined with the intrinsic speed and efficiency advantages of FPGA hardware, provides a strong foundation for future performance optimizations and large-scale applications.

4 Discussion and conclusions

In this work, we presented the co-design of hardware and software facilities for MD simulations with classical FFs on FPGA accelerators. Our implementation covers all major force components, including range-limited, bonded, and long-range electrostatics with PME, integrated within a hybrid CPU/FPGA



Table 5 Potential energy and its components of solvated DHFR using the AMBER ff99SB force field under 5 different configurations

		Potential energy (kJ mol ⁻¹)		
		FPGA	CPU	GPU
Frame 1	Bond	2087.6622	2087.8628	2087.8601
	Angle	5433.3571	5433.9008	5433.9029
	Dihedral	6907.1296	6908.4214	6908.4239
	Non-bonded	-312 340.4907	-312 345.9615	-312 345.5637
	Total	-297 910.3823	-297 915.7766	-297 915.3769
Frame 2	Bond	1907.2511	1907.1118	1907.1081
	Angle	5511.0062	5511.5854	5511.5842
	Dihedral	6927.9415	6928.6778	6928.6803
	Non-bonded	-310 742.7736	-310 748.2840	-310 747.9304
	Total	-296 395.4094	-296 400.9089	-296 400.5578
Frame 3	Bond	1928.6012	1928.7512	1928.7461
	Angle	5310.3633	5310.5181	5310.5246
	Dihedral	6755.2371	6755.8898	6755.8932
	Non-bonded	-308 428.4791	-308 434.0560	-308 433.7031
	Total	-294 433.3387	-294 438.8969	-294 438.5393
Frame 4	Bond	1922.3340	1922.4822	1922.4813
	Angle	5359.9207	5360.0319	5360.0258
	Dihedral	7027.4043	7026.7016	7026.7046
	Non-bonded	-310 148.6395	-310 154.0210	-310 153.6645
	Total	-295 839.4261	-295 844.8054	-295 844.4528
Frame 5	Bond	1947.4269	1947.2788	1947.2756
	Angle	5342.7208	5342.2733	5342.2762
	Dihedral	7001.9265	7001.2728	7001.2758
	Non-bonded	-310 775.9111	-310 781.2307	-310 780.8614
	Total	-296 485.0920	-296 490.4058	-296 490.0338

architecture. To further enhance data processing capabilities, we developed a SIMD software framework that complements the hardware modules. Through careful optimization of data flow, memory hierarchy, and compute pipelines, we achieved stable and accurate simulations ranging from simple LJ particles to a solvated protein system. Validation against CPU and GPU platforms showed close numerical agreement, and most notably, we successfully simulated DHFR in explicit water on FPGA, producing stable MD trajectories. Together, these results establish FPGAs as a feasible and energy-efficient platform for production-level MD simulations.

In terms of performance, the current FPGA implementation operates at 250 MHz, comparable to CPU execution but well below the device's theoretical ceiling of 500 MHz. This gap arises primarily from frequency limitations in the critical logic paths and bandwidth bottlenecks between compute units and the storage subsystem. Several avenues exist for improvement. One strategy is adopting a mixed-precision architecture, where non-critical computations are performed at lower precision to ease timing constraints and raise the overall clock frequency. Additional gains may be achieved by reconfiguring data paths to shorten logic depth on critical paths, thereby reducing latency, and by introducing a NoC design to improve on-chip communication efficiency among computing modules. Together, these optimizations could significantly increase sustained throughput and bring the FPGA design closer to its theoretical performance potential.

Compared with existing approaches, our FPGA implementation offers distinct advantages. Unlike general-purpose CPUs and GPUs, the FPGA's reconfigurable architecture

enables tailored pipelines for particle-particle interactions, achieving near-linear scalability when modules are duplicated. Resource utilization studies reveal that critical logic and memory resources scale predictably with system size, while careful balancing of BRAM and URAM ensures efficient use of on-chip memory. Although the performance gap relative to highly specialized ASICs such as Anton and the most-advanced GPU remains substantial, FPGA-based designs provide a unique balance between configurability, efficiency, and accuracy that makes them a possible solution for future heterogeneous HPC platforms. In principle, FPGA architectures offer deterministic latency, high energy efficiency, and customizable data paths that are potentially advantageous for irregular workloads in large-scale MD simulations. However, the current implementation is not yet fully optimized—particularly in I/O coordination and memory scheduling—and future iterations will focus on these aspects to further improve sustained throughput and close the performance gap with advanced platforms.

Several limitations also remain. Our current design is constrained by vendor FFT IPs, which support only power-of-two grid dimensions and impose fixed floating-point or fixed-point operation modes, restricting flexibility in PME calculations. More broadly, the FPGA design is developed for additive FFs such as CHARMM36m, which remain the most widely used in biomolecular simulations. However, polarizable force fields are becoming increasingly important due to their ability to capture induced-dipole effects and more realistic electrostatics.^{57–59} Implementing such polarizable FFs on FPGA presents major challenges, particularly because induced-dipole calculations require higher



precision and tighter module coupling, which place heavy demands on DSPs and memory bandwidth.⁶⁰ The Drude FF, based on the classical Drude oscillator model and an extended Lagrangian formalism, could be more straightforward to implement in our FPGA design.⁶¹ Machine learning potentials or machine learning force fields (MLFFs) are also rapidly emerging,^{62,63} such as ANI,^{64,65} DeepMD,^{66–68} and the MACE series.^{69,70} However, MLFFs are still significantly slower than additive and polarizable FFs. Their implementation on FPGA remains an interesting but challenging future direction due to their irregular memory access and heavy reliance on tensor operations.

We note that in our current FPGA implementation, the computation of non-bonded interactions, particularly the PME electrostatics, remains a major bottleneck. Alternative algorithms such as the Fast Multipole Method (FMM) could offer advantages by reducing communication overhead through hierarchical decomposition.⁷¹ Beyond deterministic algorithms, stochastic approaches have recently emerged as powerful alternatives to address the communication and synchronization limitations inherent to FFT-based methods. In particular, the Random Batch Ewald (RBE) method employs stochastic mini-batch sampling to speed up the summation of the Fourier series in the calculation of E_{rec} (eqn (8)), achieving exceptional parallel scalability on large CPU clusters.^{72–75} The simplified communication patterns and locality-friendly characteristics of these hierarchical and stochastic methods make them highly appealing for future implementation on specialized hardware such as FPGAs, where they may provide a transformative route to alleviating the von Neumann bottleneck in exascale MD simulations.

In conclusion, our study demonstrates that FPGA accelerators can deliver accurate, stable, and scalable MD simulations of biomolecular systems. While further optimization is needed, the demonstrated feasibility, efficiency, and adaptability of FPGA hardware establish a strong foundation for future advances in large-scale biomolecular simulations, bridging the gap between current CPU/GPU platforms and next-generation domain-specific accelerators. This proof-of-concept hybrid CPU/FPGA design highlights the feasibility of dedicated hardware for accelerating scientific computing and points toward future development of computing infrastructure that can extend the applicable scale of MD simulations.

Author contributions

Jing Xiao: methodology, investigation, software, formal analysis, validation, visualization, writing – original draft, and writing – review and editing. Jinfeng Chen: methodology, investigation, software, formal analysis, validation, visualization and writing – review and editing. Ye Ding: methodology, software, investigation, validation, and formal analysis. You Xu: methodology, supervision, and writing – review and editing. Jing Huang: conceptualization, funding acquisition, methodology, project administration, resources, supervision, and writing – review and editing.

Conflicts of interest

There are no conflicts to declare.

Data availability

The Verilog HDL code for molecular dynamics simulation (deployed on the Inspur F37x), together with the host-side C++ program controlling the Inspur F37x accelerator card, is publicly available as an archived and citable release on Zenodo at <https://doi.org/10.5281/zenodo.18096184>, which corresponds to the GitHub repository <https://github.com/JingHuangLab/FPGA-MD-code-and-data>. The repository includes specifications, dependencies, and detailed instructions for building, synthesizing, and executing the simulations. Representative input files and corresponding output data for key benchmarks are also provided in the GitHub repository, while larger trajectories and benchmark datasets have been deposited on Zenodo and are publicly available at <https://doi.org/10.5281/zenodo.17796179>.

Supplementary information (SI) is available. See DOI: <https://doi.org/10.1039/d5dd00391a>.

Acknowledgements

This work was supported by the Shandong Provincial Natural Science Foundation (ZR2024LZH009), the “Pioneer” and “Leading Goose” R&D Program of Zhejiang (2023C03109, 2024SSYS0036), the National Natural Science Foundation of China (32171247), and the State Key Laboratory of Gene Expression. We thank the Westlake University Supercomputer Center and the Inspur for computational resources and related assistance.

Notes and references

- 1 L. Donaldson, *Mater. Today*, 2013, **16**, 360.
- 2 M. De Vivo, M. Masetti, G. Bottegoni and A. Cavalli, *J. Med. Chem.*, 2016, **59**, 4035–4061.
- 3 R. Qian, J. Xue, Y. Xu and J. Huang, *J. Chem. Inf. Model.*, 2024, **64**, 7214–7237.
- 4 S. Jiang, J. Zhang, K. Diao, X. Liu and Z. Ding, *Adv. Funct. Mater.*, 2025, **35**, 2423566.
- 5 W. E and E. Vanden-Eijnden, *Annu. Rev. Phys. Chem.*, 2010, **61**, 391–420.
- 6 X. Lu and J. Huang, *Biophys. J.*, 2024, **123**, 1195–1210.
- 7 X. Li, X. Yang, X. Lu, B. Lin, Y. Zhang, B. Huang, Y. Zhou, J. Huang, K. Wu, Q. Zhou, *et al.*, *Nat. Commun.*, 2025, **16**, 7600.
- 8 G. Kumar, R. R. Mishra and A. Verma, in *Introduction to Molecular Dynamics Simulations*, ed. A. Verma, S. Mavinkere Rangappa, S. Ogata and S. Siengchin, Springer Nature Singapore, Singapore, 2022, pp. 1–19.
- 9 W. Hwang, S. L. Austin, A. Blondel, E. D. Boittier, S. Boresch, M. Buck, J. Buckner, A. Caflisch, H.-T. Chang, X. Cheng, Y. K. Choi, J.-W. Chu, M. F. Crowley, Q. Cui, A. Damjanovic, Y. Deng, M. Devereux, X. Ding, M. F. Feig,



- J. Gao, D. R. Glowacki, J. E. I. Gonzales, M. B. Hamaneh, E. D. Harder, R. L. Hayes, J. Huang, Y. Huang, P. S. Hudson, W. Im, S. M. Islam, W. Jiang, M. R. Jones, S. Käser, F. L. Kearns, N. R. Kern, J. B. Klauda, T. Lazaridis, J. Lee, J. A. Lemkul, X. Liu, Y. Luo, A. D. J. MacKerell, D. T. Major, M. Meuwly, K. Nam, L. Nilsson, V. Ovchinnikov, E. Paci, S. Park, R. W. Pastor, A. R. Pittman, C. B. Post, S. Prasad, J. Pu, Y. Qi, T. Rathinavelan, D. R. Roe, B. Roux, C. N. Rowley, J. Shen, A. C. Simmonett, A. J. Sodt, K. Töpfer, M. Upadhyay, A. van der Vaart, L. I. Vazquez-Salazar, R. M. Venable, L. C. Warrensford, H. L. Woodcock, Y. Wu, C. L. I. Brooks, B. R. Brooks and M. Karplus, *J. Phys. Chem. B*, 2024, **128**, 9976–10042.
- 10 R. Salomon-Ferrer, A. W. Götz, D. Poole, S. Le Grand and R. C. Walker, *J. Chem. Theory Comput.*, 2013, **9**, 3878–3888.
- 11 J. C. Phillips, D. J. Hardy, J. D. C. Maia, J. E. Stone, J. V. Ribeiro, R. C. Bernardi, R. Buch, G. Fiorin, J. Hénin, W. Jiang, R. McGreevy, M. C. R. Melo, B. K. Radak, R. D. Skeel, A. Singharoy, Y. Wang, B. Roux, A. Aksimentiev, Z. Luthey-Schulten, L. V. Kalé, K. Schulten, C. Chipot and E. Tajkhorshid, *J. Chem. Phys.*, 2020, **153**, 044130.
- 12 P. Eastman, R. Galvelis, R. P. Peláez, C. R. A. Abreu, S. E. Farr, E. Gallicchio, A. Gorenko, M. M. Henry, F. Hu, J. Huang, A. Krämer, J. Michel, J. A. Mitchell, V. S. Pande, J. P. Rodrigues, J. Rodriguez-Guerra, A. C. Simmonett, S. Singh, J. Swails, P. Turner, Y. Wang, I. Zhang, J. D. Chodera, G. De Fabritiis and T. E. Markland, *J. Phys. Chem. B*, 2024, **128**, 109–116.
- 13 M. J. Abraham, T. Murtola, R. Schulz, S. Pall, J. C. Smith, B. Hess and E. Lindahl, *SoftwareX*, 2015, **1–2**, 19–25.
- 14 D. Jones, J. E. Allen, Y. Yang, W. F. Drew Bennett, M. Gokhale, N. Moshiri and T. S. Rosing, *J. Chem. Theory Comput.*, 2022, **18**, 4047–4069.
- 15 P. Hamm, *J. Chem. Phys.*, 2025, **162**, 054108.
- 16 C. Wu, T. Geng, A. Guo, S. Bandara, P. Haghi, C. Liu, A. Li and M. Herbordt, *Proceedings of the International Conference for High Performance Computing, Networking, Storage and Analysis*, New York, NY, USA, 2023.
- 17 J. M. Rodriguez-Borbon, A. Kalantar, S. S. R. K. Yamijala, M. B. Oviedo, W. Najjar and B. M. Wong, *J. Chem. Theory Comput.*, 2020, **16**, 2085–2098.
- 18 C. Yang, T. Geng, T. Wang, R. Patel, Q. Xiong, A. Sanaullah, C. Wu, J. Sheng, C. Lin, V. Sachdeva, W. Sherman and M. Herbordt, *Proceedings of the International Conference for High Performance Computing, Networking, Storage and Analysis*, New York, NY, USA, 2019, pp. 1–31.
- 19 T. Narumi, K. Yasuoka, M. Taiji, F. Zerbetto and S. Höfinger, *Comput. J.*, 2011, **54**, 1181–1187.
- 20 G. Morimoto, Y. M. Koyama, H. Zhang, T. S. Komatsu, Y. Ohno, K. Nishida, I. Ohmura, H. Koyama and M. Tajit, *SC21: International Conference for High Performance Computing, Networking, Storage and Analysis*, 2021, pp. 1–15.
- 21 D. E. Shaw, M. M. Deneroff, R. O. Dror, J. S. Kuskin, R. H. Larson, J. K. Salmon, C. Young, B. Batson, K. J. Bowers, J. C. Chao, M. P. Eastwood, J. Gagliardo, J. P. Grossman, C. R. Ho, D. J. Ierardi, I. Kolossváry, J. L. Klepeis, T. Layman, C. McLeavey, M. A. Moraes, R. Mueller, E. C. Priest, Y. Shan, J. Spengler, M. Theobald, B. Towles and S. C. Wang, *Commun. ACM*, 2008, **51**, 91–97.
- 22 D. E. Shaw, J. Grossman, J. A. Bank, B. Batson, J. A. Butts, J. C. Chao, M. M. Deneroff, R. O. Dror, A. Even, C. H. Fenton, A. Forte, J. Gagliardo, G. Gill, B. Greskamp, C. R. Ho, D. J. Ierardi, L. Iserovich, J. S. Kuskin, R. H. Larson, T. Layman, L.-S. Lee, A. K. Lerer, C. Li, D. Killebrew, K. M. Mackenzie, S. Y.-H. Mok, M. A. Moraes, R. Mueller, L. J. Nociolo, J. L. Peticolas, T. Quan, D. Ramot, J. K. Salmon, D. P. Scarpazza, U. B. Schafer, N. Siddique, C. W. Snyder, J. Spengler, P. T. P. Tang, M. Theobald, H. Toma, B. Towles, B. Vitale, S. C. Wang and C. Young, *SC'14: Proceedings of the International Conference for High Performance Computing, Networking, Storage and Analysis*, 2014, pp. 41–53.
- 23 D. E. Shaw, P. J. Adams, A. Azaria, J. A. Bank, B. Batson, A. Bell, M. Bergdorf, J. Bhatt, J. A. Butts, T. Correia, R. M. Dirks, R. O. Dror, M. P. Eastwood, B. Edwards, A. Even, P. Feldmann, M. Fenn, C. H. Fenton, A. Forte, J. Gagliardo, G. Gill, M. Gorlatova, B. Greskamp, J. Grossman, J. Gullingsrud, A. Harper, W. Hasenplaugh, M. Heily, B. C. Heshmat, J. Hunt, D. J. Ierardi, L. Iserovich, B. L. Jackson, N. P. Johnson, M. M. Kirk, J. L. Klepeis, J. S. Kuskin, K. M. Mackenzie, R. J. Mader, R. McGowen, A. McLaughlin, M. A. Moraes, M. H. Nasr, L. J. Nociolo, L. O'Donnell, A. Parker, J. L. Peticolas, G. Pocina, C. Predescu, T. Quan, J. K. Salmon, C. Schwink, K. S. Shim, N. Siddique, J. Spengler, T. Szalay, R. Tabladillo, R. Tartler, A. G. Taube, M. Theobald, B. Towles, W. Vick, S. C. Wang, M. Wazlowski, M. J. Weingarten, J. M. Williams and K. A. Yuh, *Proceedings of the International Conference for High Performance Computing, Networking, Storage and Analysis*, New York, NY, USA, 2021.
- 24 A. George, H. Lam and G. Stitt, *Comput. Sci. Eng.*, 2011, **13**, 82–86.
- 25 A. D. George, M. C. Herbordt, H. Lam, A. G. Lawande, J. Sheng and C. Yang, *2016 IEEE High Performance Extreme Computing Conference*, HPEC, 2016, pp. 1–7.
- 26 A. M. Cabrera, Y. A. Yucasan, F. Y. Liu, W. Blokland and J. S. Vetter, *2023 IEEE High Performance Extreme Computing Conference*, HPEC, 2023, pp. 1–6.
- 27 S. Kilts, *Advanced FPGA Design: Architecture, Implementation, and Optimization*, Wiley-IEEE Press, 2007.
- 28 H. M. Waidysooriya, M. Hariyama and K. Kasahara, *2016 IEEE/ACIS 15th International Conference on Computer and Information Science (ICIS)*, 2016, pp. 1–5.
- 29 L. C. Stewart, C. Pascoe, E. Davis, B. W. Sherman, M. Herbordt and V. Sachdeva, *2021 IEEE 29th Annual International Symposium on Field-Programmable Custom Computing Machines (FCCM)*, 2021, pp. 270.
- 30 Y. Yang, W. Long, R. Kannan and V. K. Prasanna, *2023 33rd International Conference on Field-Programmable Logic and Applications (FPL)*, 2023, pp. 174–181.



- 31 M. Choi, X. Xu and V. Moroz, *2019 18th IEEE Intersociety Conference on Thermal and Thermomechanical Phenomena in Electronic Systems (ITherm)*, 2019, pp. 107–112.
- 32 U. Khan, H. Owen and J. Hughes, *Sixth Annual IEEE International ASIC Conference and Exhibit*, 1993, pp. 336–340.
- 33 C. Yang, T. Geng, T. Wang, R. Patel, Q. Xiong, A. Sanaullah, J. Sheng, C. Lin, V. Sachdeva, W. Sherman and M. C. Herbordt, *arXiv*, 2019, preprint, arXiv:1905.05359, DOI: [10.48550/arXiv.1905.05359](https://doi.org/10.48550/arXiv.1905.05359).
- 34 N. Fujita, R. Kobayashi, Y. Yamaguchi and T. Boku, *2021 IEEE International Conference on Cluster Computing (CLUSTER)*, 2021, pp. 783–786.
- 35 D. Winterberg, V. Kumar, T. Chen and B. Mutnury, *2023 Joint Asia-Pacific International Symposium on Electromagnetic Compatibility and International Conference on ElectroMagnetic Interference & Compatibility, APEMC/INCEMIC*, 2023, pp. 1–4.
- 36 K. Vanommeslaeghe and A. MacKerell, *Biochim. Biophys. Acta Gen. Subj.*, 2015, **1850**, 861–871.
- 37 NVIDIA Corporation, *NVIDIA A100 Tensor Core GPU Architecture*, NVIDIA Corporation, 2020.
- 38 D. C. Rapaport, *The Art of Molecular Dynamics Simulation*, Cambridge University Press, 2nd edn, 2004.
- 39 X. Lu, J. Chen and J. Huang, *Structure*, 2025, **33**, 1138–1149.
- 40 K. J. Bowers, R. O. Dror and D. E. Shaw, *J. Comput. Phys.*, 2007, **221**, 303–329.
- 41 S. Jayaraman, B. Zhang and V. Prasanna, *2022 International Conference on Field-Programmable Technology (ICFPT)*, 2022, pp. 1–11.
- 42 C. Wu, T. Geng, S. Bandara, C. Yang, V. Sachdeva, W. Sherman and M. Herbordt, *2021 IEEE 29th Annual International Symposium on Field-Programmable Custom Computing Machines (FCCM)*, 2021, pp. 142–151.
- 43 IEEE Computer Society, *IEEE Standard for Floating-Point Arithmetic*, IEEE Std 754-2019 (Revision of IEEE 754-2008), 2019, pp. 1–84, DOI: [10.1109/IEEESTD.2019.8766229](https://doi.org/10.1109/IEEESTD.2019.8766229).
- 44 E. R. Overchick and B. Abramov, *2014 IEEE 28th Convention of Electrical & Electronics Engineers in Israel (IEEEI)*, 2014, pp. 1–5.
- 45 J. Villarreal and W. A. Najjar, *2008 International Conference on Field Programmable Logic and Applications*, 2008, pp. 667–670.
- 46 C. Yang, T. Geng, T. Wang, C. Lin, J. Sheng, V. Sachdeva, W. Sherman and M. Herbordt, *2019 IEEE 30th International Conference on Application-specific Systems, Architectures and Processors (ASAP)*, 2019, pp. 263–271.
- 47 M. Chiu and M. C. Herbordt, *ACM Trans. Reconfigurable Technol. Syst.*, 2010, **3**, 1–37.
- 48 T. A. Darden, D. M. York and L. G. Pedersen, *J. Chem. Phys.*, 1993, **98**, 10089–10092.
- 49 Z.-H. Duan and R. Krasny, *J. Chem. Phys.*, 2000, **113**, 3492–3495.
- 50 B. S. C. Varma, K. Paul and M. Balakrishnan, *2013 26th International Conference on VLSI Design and 2013 12th International Conference on Embedded Systems*, 2013, pp. 92–97.
- 51 K. Aatish and B. Zhang, Three Dimensional Fast Fourier Transform CUDA Implementation, in *CSE 260: Parallel Computation (Fall 2012)*, University of California, San Diego, 2013, https://cseweb.ucsd.edu/~baden/classes/Exemplars/cse260_fa12/3DFFT.pdf.
- 52 P. Eastman, J. Swails, J. D. Chodera, R. T. McGibbon, Y. Zhao, K. A. Beauchamp, L.-P. Wang, A. C. Simmonett, M. P. Harrigan, C. D. Stern, R. P. Wiewiora, B. R. Brooks and V. S. Pande, *PLoS Comput. Biol.*, 2017, **13**, 1–17.
- 53 J. Sheng, C. Yang, A. Sanaullah, M. Papamichael, A. Caulfield and M. C. Herbordt, *2017 27th International Conference on Field Programmable Logic and Applications (FPL)*, 2017, pp. 1–4.
- 54 Y. Gu, T. VanCourt and M. Herbordt, *International Conference on Field Programmable Logic and Applications*, 2005, pp. 475–480.
- 55 P. Eastman, R. Galvelis, R. P. Peláez, C. R. A. Abreu, S. E. Farr, E. Gallicchio, A. Gorenko, M. M. Henry, F. Hu, J. Huang, A. Krämer, J. Michel, J. A. Mitchell, V. S. Pande, J. P. Rodrigues, J. Rodriguez-Guerra, A. C. Simmonett, S. Singh, J. Swails, P. Turner, Y. Wang, I. Zhang, J. D. Chodera, G. De Fabritiis and T. E. Markland, *J. Phys. Chem. B*, 2024, **128**, 109–116.
- 56 V. Hornak, R. Abel, A. Okur, B. Strockbine, A. Roitberg and C. Simmerling, *Proteins: Struct., Funct., Bioinf.*, 2006, **65**, 712–725.
- 57 J. Deng and Q. Cui, *J. Am. Chem. Soc.*, 2022, **144**, 4594–4610.
- 58 J. Chen, Z. Qiu and J. Huang, *ACS Omega*, 2023, **8**, 42936–42950.
- 59 Z. Pan, J. Huang and W. Zhuang, *JACS Au*, 2021, **1**, 1788–1797.
- 60 Z. Huang, S. Zhao, P. Cieplak, Y. Duan, R. Luo and H. Wei, *J. Chem. Theory Comput.*, 2023, **19**, 5047–5057.
- 61 J. Huang, J. A. Lemkul, P. K. Eastman and A. D. MacKerell Jr, *J. Comput. Chem.*, 2018, **39**, 1682–1689.
- 62 Y. Ding, K. Yu and J. Huang, *Curr. Opin. Struct. Biol.*, 2023, **78**, 102502.
- 63 X. Feng, Y. Xu and J. Huang, *Commun. Comput. Chem.*, 2025, **7**, 152–160.
- 64 J. S. Smith, O. Isayev and A. E. Roitberg, *Chem. Sci.*, 2017, **8**, 3192–3203.
- 65 C. Devereux, J. S. Smith, K. K. Huddleston, K. Barros, R. Zubatyuk, O. Isayev and A. E. Roitberg, *J. Chem. Theory Comput.*, 2020, **16**, 4192–4202.
- 66 H. Wang, L. Zhang, J. Han and W. E, *Comput. Phys. Comm.*, 2018, **228**, 178–184.
- 67 J. Zeng, D. Zhang, D. Lu, P. Mo, Z. Li, Y. Chen, M. Rynik, L. Huang, Z. Li, S. Shi, Y. Wang, H. Ye, P. Tuo, J. Yang, Y. Ding, Y. Li, D. Tisi, Q. Zeng, H. Bao, Y. Xia, J. Huang, K. Muraoka, Y. Wang, J. Chang, F. Yuan, S. L. Bore, C. Cai, Y. Lin, B. Wang, J. Xu, J.-X. Zhu, C. Luo, Y. Zhang, R. E. A. Goodall, W. Liang, A. K. Singh, S. Yao, J. Zhang, R. Wentzcovitch, J. Han, J. Liu, W. Jia, D. M. York, W. E, R. Car, L. Zhang and H. Wang, *J. Chem. Phys.*, 2023, **159**, 054801.
- 68 J. Zeng, D. Zhang, A. Peng, X. Zhang, S. He, Y. Wang, X. Liu, H. Bi, Y. Li, C. Cai, C. Zhang, Y. Du, J.-X. Zhu, P. Mo,



- Z. Huang, Q. Zeng, S. Shi, X. Qin, Z. Yu, C. Luo, Y. Ding, Y.-P. Liu, R. Shi, Z. Wang, S. L. Bore, J. Chang, Z. Deng, Z. Ding, S. Han, W. Jiang, G. Ke, Z. Liu, D. Lu, K. Muraoka, H. Oliaei, A. K. Singh, H. Que, W. Xu, Z. Xu, Y.-B. Zhuang, J. Dai, T. J. Giese, W. Jia, B. Xu, D. M. York, L. Zhang and H. Wang, *J. Chem. Theory Comput.*, 2025, **21**, 4375–4385.
- 69 I. Batatia, D. P. Kovacs, G. N. C. Simm, C. Ortner and G. Csanyi, *Adv. Neural Inf. Process. Syst.*, 2022, **35**, 11423–11436.
- 70 D. P. Kovacs, J. H. Moore, N. J. Browning, I. Batatia, J. T. Horton, Y. Pu, V. Kapil, W. C. Witt, I.-B. Magdau, D. J. Cole and G. Csanyi, *J. Am. Chem. Soc.*, 2025, **147**, 17598–17611.
- 71 B. Kohnke, C. Kutzner and H. Grubmüller, *J. Chem. Theory Comput.*, 2020, **16**, 6938–6949.
- 72 S. Jin, L. Li, Z. Xu and Y. Zhao, *SIAM J. Sci. Comput.*, 2021, **43**, B937–B960.
- 73 J. Liang, Z. Xu and Y. Zhao, *J. Phys. Chem.*, 2022, **126**, 3583–3593.
- 74 J. Liang, P. Tan, Y. Zhao, L. Li, S. Jin, L. Hong and Z. Xu, *J. Chem. Phys.*, 2022, **156**, 014114.
- 75 J. Liang, P. Tan, L. Hong, S. Jin, Z. Xu and L. Li, *J. Chem. Phys.*, 2022, **157**, 144102.

